Pontes, P, Gonçalves, I, Andredaki, M, Georgoulas, A, Moreira, ALN and Moita, AS

Fluid flow and heat transfer in microchannel devices for cooling applications: Experimental and numerical approaches

Fluid Flow and Heat Transfer in Microchannel Devices for Cooling Applications: Experimental and Numerical Approaches.

P. Pontes[1], I. Gonçalves[1], M. Andredaki[2], A. Georgoulas[2], A.L.N. Moreira[1] and A.S. Moita[1,3*]

1: IN+ Center for Innovation, Technology and Policy Research, Instituto Superior Técnico, Universidade de Lisboa, Portugal

2: Advanced Engineering Centre, School of Architecture Technology and Engineering, Cockcroft Building, Lewes Road, University of Brighton BN2 4GJ, UK

3: CINAMIL – Centro de Investigação Desenvolvimento e Inovação da Academia Militar, Academia Militar, Instituto Universitário Militar, Lisboa, Portugal

*Email: anamoita@tecnico.ulisboa.pt moita.asoh@exercito.pt

Abstract

Microchannel heat sinks are pointed to have a great potential in cooling systems. This paper presents a systematic study to develop a microchannel heat sink to be used in cooling applications. Particular emphasis is given to PV panels cooling. A systematic experimental approach is used to optimize the heat sink geometry. Then the potential advantage of using flow boiling conditions is explored in both numerical and experimental approaches. The

two-phase flow is characterized in two different sets of conditions. In the experimental approach, a constrained bubble flow was observed with a stable pattern and bubble frequency in the narrower channel. In the wider channel a bubbly flow was observed with increased bubble diameters. Numerical simulations were also performed in order to examine the first transient stages of the two-phase flow development close to the inlet of the considered microchannels assuming an initial arbitrary distribution of nucleation sites. For this purpose, a previously developed and validated numerical simulation framework was utilised. The proposed customized tool has been developed in the general context of OpenFOAM CFD Toolbox and it accounts for phase-change (boiling/condensation) as well as for Conjugate Heat Transfer between solid and two-phase flow domains. The numerical predictions reveal that the proposed tool is sensitive enough to capture the effects of channel aspect ratio, applied heat flux and applied mass flux on the generated transient bubble dynamics and the associated heat transfer characteristics and it can constitute an important tool for quantifying the underpinned complex physical mechanisms, providing further insight into the experimental observations and measurements.

1. Introduction

High Concentration Photovoltaic (HCPV) Panels are one of the most efficient photovoltaic technologies in converting solar energy to electricity [1]. These allow a higher concentration of energy in a multijunction cell which can reach standard efficiencies of up to 40%. This higher concentration is also the cause

of the higher working temperatures of these cells, known to penalize conversion efficiency [2]. To address this, an appropriate cooling solution is needed in these types of panels. Currently in use, passive cooling methods are reliable, don't consume system energy and are cheap to manufacture but they lack in performance [3]. Alternatively active cooling systems could be used to improve these systems. Microchannel cooling systems are one of the suiting options due to the small scale and high reported heat dissipation.

Since they were first proposed by Tuckerman and Pease [4], microchannel heat sinks have been progressively optimized to get the most out of them. For instance, the geometrical optimization of these devices has been carried out by several authors to improve their heat transfer while keeping pressure losses low in the channels. These studies, such as the ones carried out by Peng et al. [5], Xia [6] or Wang [7] tried to establish relationships between the channel geometries and its performance, creating design guidelines. Raghuraman *et al.* [8] performed a numerical and experimental work where they studied the influence of the aspect ratio on thermal performance using a heat exchanger with rectangular channels. The three heat exchangers tested have an aspect ratio of 20, 30, and 46.6. Through experimental and numerical tests, the results obtained included the parameters of pressure drop, friction factor, Nusselt number, thermal resistance, pumping power, and Poiseuille number, Raghuraman *et al.* [8] concluded that it is preferable to implement the exchanger with intermediate dimensions since it was responsible for removing a greater amount of heat, while keeping the other parameters at a level that is feasible for the project. Upadhye and Kandlikar [9] carried out

numerical work to evaluate the effect of the heat exchanger geometry to cool an electronic chip with dimensions of 25mm by 25mm. For an imposed flow of 100 /cm^2, they concluded that a channel. with smaller dimensions depicts a better cooling performance. Wang *et al.* [7] tested microchannels with a rectangular, trapezoidal, and triangular section, concluding that channels with a higher aspect ratio and smaller hydraulic diameter have a lower thermal resistance but a greater pressure drop. Wang *et al.* [7] also concluded that with the increase in the number of channels, the thermal resistance decreases, but in return, there will be an increase in the pressure drop in the exchanger. Xie *et al.* [9] tested an exchanger with minichannels to cool an area of 20 mm x 20 mm, concluding that narrower channels have a better performance, balancing heat transfer and pressure drop, when compared to wider channels.

All the aforementioned studies were performed with single-phase fluid flows. By allowing the refrigerant to boil, the latent heat of the fluid is used to increase the heat flux removed. Despite presenting this added value, multiphase flow is more difficult to model, predict and control. Hetsroni *et al.* [10] conducted an experimental investigation on the effect of boiling on the cooling of electronic devices, using Vertrel XF as a boiling refrigerant, and finally compared it with the results obtained using water. The temperature gradient using boiling did not exceed 5K, while in water cooling the temperature difference was 20 K. However, the growth and consequent collapse of the vapor bubbles caused fluctuations in the pressure drop and decreased the heat transfer coefficient. In the work carried out by Tran *et al.*

[11] it was concluded that in smaller channels, the nucleation mechanism is dominant compared to the convection mechanism, thus concluding that boiling in microchannels increases heat transfer.

The brief literature review performed here shows a wide range of studies on flow boiling heat transfer in microchannels. However, geometry optimization (balancing heat transfer and pressure drops) is mostly taken by a trial-and-error approach and the potential advantages of using boiling to enhance the heat transfer are not clearly presented, as they are presented against many obstacles.

In this work a single channel experimental approach is used to single out the effects of flow boiling in the pressure drop considering different channel widths. A previously validated numerical simulation framework for boiling flows is then applied to replicate 2 experimental conditions aiming to assess the first transient stages of the bubble growth dynamics at the first stages of the two-phase flow development in each case, considering the inlet regions of the considered micro-channels. The local and global heat transfer characteristics are also exported from the numerical predictions together with the bubble growth dynamics, providing further insight about the physics and phenomena occurring inside the channels, expanding our knowledge on how to optimize them. It is worth mentioning that although the imposed working conditions are more focused on a cooling strategy to be implemented in PV channels, the conclusions taken here are useful in a wider range of engineering applications. PDMS channels are flexible, inexpensive polymeric material, which can be used in a growing industry of wearables. For instance,

thermal management strategies have been studied in applications for sports equipment, in airspace industry and in defense industry, namely in NBQ suits e.g. [12-14]. The few existing solutions based on liquid cooling address a complex tubes system, which requires a pump that may increase the weight of the equipment up to 10kg [15]. The use of flexible and inexpensive microchannel based heat sinks may also work as a game changer for this field of application.

2. Experimental Methodology

To infer on the effect of the channel width in the boiling process, single channel prototypes were manufactured in Poly(dimethylsiloxane) – PDMS and tested. The manufacturing process is described in the following sub-section.

2.1. Manufacturing the channel prototypes

The tested channels are manufactured by pouring liquid PDMS on a resin 3D printed mold. Various molds were manufactured as to account for a given range of channel widths. For this work two different channel widths ($W_{channel}$) were used, namely 0.5 mm and 1 mm. The geometry of the mold is represented in Figure 1. The channels section is square.

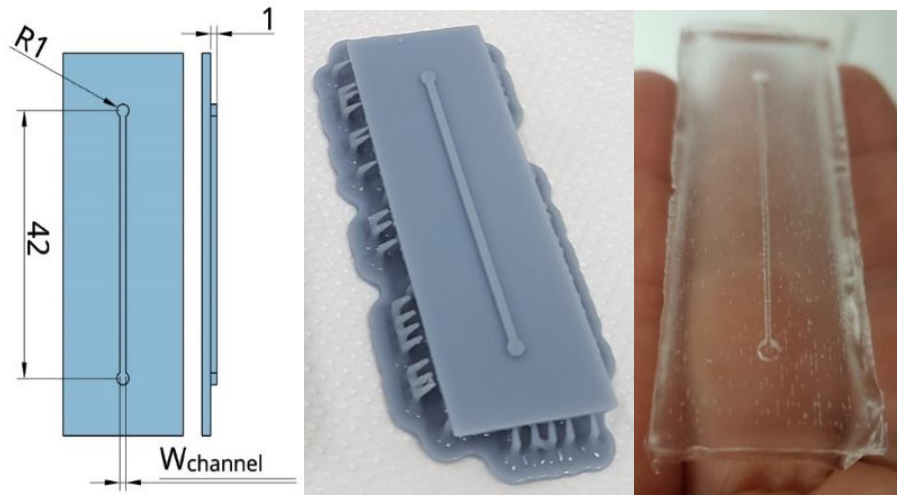

*Figure 1 – **A.** Drawing of the prototype mold (dimensions in mm); **B.** 3D printed mold; **C.** PDMS single channel prototype*

After the mold is printed, it is closed with aluminum tape and filled with 4g of PDMS. The PDMS is then left to cure for 48h in a closed chamber, at room temperature. During this time air bubbles trapped inside of the PDMS escape and the prototype turns solid. Finally, it is cut to size and it is punctured in the inlet and outlet of the channel so that liquid can flow through it.

2.2. Experimental Setup

A schematic of the used setup is seen in Figure 2 a). When the prototype is ready, it is placed on the setup. The PDMS device (5) is placed on top of a stainless-steel foil (AISI 304) (8) and tightened between two acrylic plates, to properly seal. The stainless-steel foil is connected to a HP 6274B DC power source (6), to be heated by Joule effect. A detailed depiction of this part is presented in Figure 2 b). The flowrate is controlled using a syringe pump (1) that pumps the fluid to the microchannel. The working fluid is preheated

using a sleeve heater wrapped around the syringe HARVARD (2). The temperature is controlled with K thermocouples in the sleeve, connected to a control unit, using an on-off method (3). The inlet and outlet conditions are then measured using K thermocouples and absolute pressure transducers (Wika A-10). The pressure transducer at the inlet measures up to 250kPa, while the pressure transducer at the outlet measures up to 160kPa. The data from these sensors is read by a data acquisition board and processed using a house-made LabVIEW routine. The flow boiling inside of the microchannel is visualized and recorded during the experiments using a Phantom v4.2 High Speed Camera (4), working at 1000fps. The camera uses a Leica microscope lens with 4x magnification. For the optical configuration used here the calibration factor is 21μm/pixel.

Finally, the working fluid exits the system and is stored in a container at atmospheric pressure.

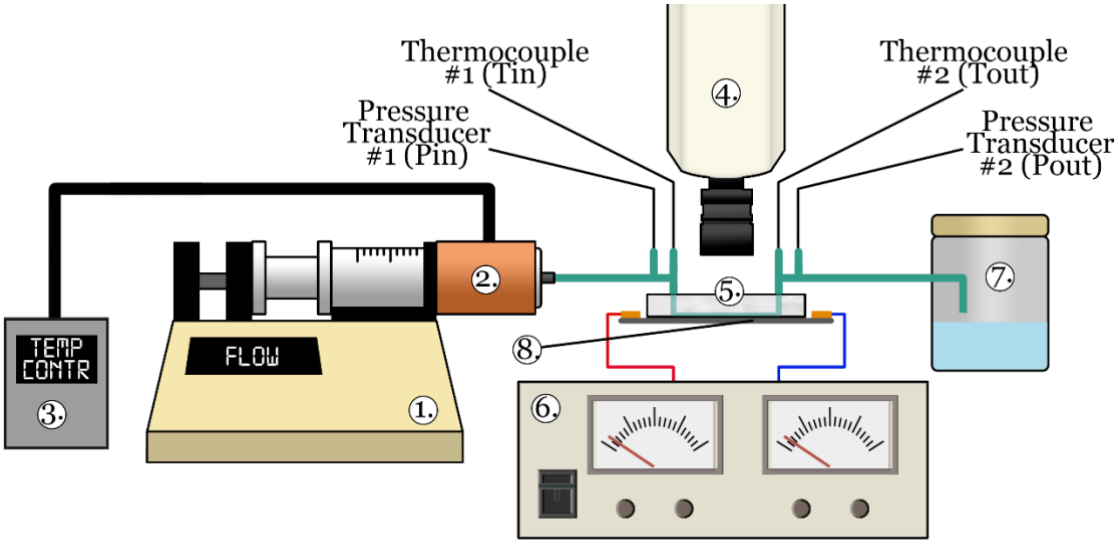

(a)

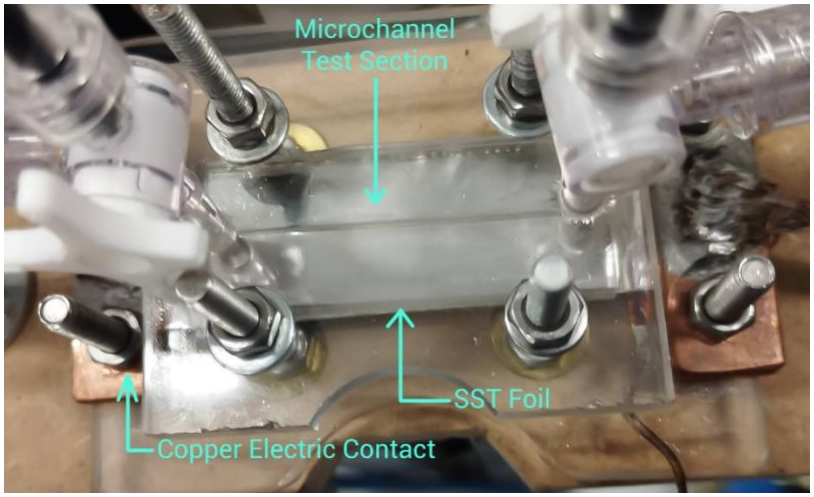

(b)

Figure 2 – a) Experimental Setup Schematic: 1. Syringe Pump, 2. Syringe Heater, 3. Temperature Control for the syringe heater, 4. High-Speed Camera, 5. PDMS microchannel device, 6. DC Power Output, 7. Container for fluid exiting the system, 8. Stainless-Steel Foil. b) Close up of the test section.

2.3. Surface Characterization

To obtain closer input conditions for the simulation, both the surface of the PDMS and the Stainless-Steel foil were characterized using a tensiometer

(THETA, from Attention), which was used to measure static and quasi-static (advancing and receding) contact angles, using the sessile drop method. The values depicted in Table 1 result from an average of 5-7 measurements along the sample surfaces, so that the average values can be representative of the entire surface. Details on the measurement procedures are given in previous work [16,17].

Table 1 - Material Surfaces Contact Angles

	PDMS	Stainless Steel
Static Contact Angle(º) θ:	102.6	64.2
Quasi-static Contact Angle(º):		
Advancing θ_a	110.9	76.1
Receding θ_r	75.7	34.4

2.4. Experimental procedure and conditions

Before the experiment is run, the syringe is filled with the working fluid HFE 7100. The relevant properties of this fluid are presented in the table below [18]:

Table 2 - HFE7100 Fluid Properties

HFE7100	
Saturation Temperature (ºC)	61
Surface Tension [N/m]	14
hlv [m^2/s^2]	125.6
Liquid Properties:	
Density [kg/m^3]	1500
Dynamic Viscosity [mN s/m^2]	0.279
Specific Heat Capacity [J/kg K]	1183
Conductivity [W/m K]	0.07
Vapor Properties:	
Density [kg/m^3]	9,6
Specific Heat Capacity [J/kg K]	1260
Conductivity [W/m K]	0.063

To perform the experiment, the syringe is preheated to 50ºC. After that, a given current is fed through the stainless-steel foil. This current is measured with a multimeter and calculated based on the desired heat flux. The temperature of the foil is controlled with a thermocouple so that one can know when a stable temperature is reached. Once the pump starts working, the fluid should reach stable pressure and temperature results. Once we have a stable flow, the pressure and temperature data are recorded at the same time

the high-speed video is. These steps are repeated for each set of conditions and repeated 3 times for each individual set. In this work, and in order to validate the numerical results, two set cases were chosen. **The conditions of the two established experimental cases were selected so they represent two extremes, with considerably different heat and mass fluxes and channel width, in order to examine the sensitivity of the numerical simulation framework on capturing the difference in the resulted two-phase flow and heat transfer characteristics. These conditions for each set are presented in the table below**:

Table 3 - Test case conditions

Case	Heat Flux [W/m² K]	Flowrate [ml/min]	Channel Width [μm]	Re
1	1695.88	10.125	500	900.00
2	2403.46	4.56	1000	304.00

2.5. Data processing and uncertainty analysis

The fluid flow inside the microchannel is characterized as a laminar flow, with values of the Reynolds number, Re=900 and Re=304, for the flow rates of 10.125 and 4.56 ml/min, respectively. Here $Re=\rho u D_h/\mu$, where ρ and μ and the specific mass and dynamic viscosity of the working fluid and Dh is the hydraulic diameter. The main stream average velocity u is given by mass conservation, using the volumetric flow rate values.

The flow is within the bubbly flow regime. Bubble dynamics was addressed and assessed based on image analysis. To evaluate bubble velocity, the high-speed camera videos were analyzed with the aim to find isolated bubble nucleations. Once the bubble has separated the surface, it is tracked until it leaves the camera view range. For each 15 frames, the bubble's center position is registered in a spreadsheet, using its pixel coordinates. An approximate diameter in pixels is also registered in the spreadsheet. Both the center of the bubble and its diameter are extracted by visual analysis with the aid of the camera's software to perform the measurements, so an accuracy of ±1 pixel was considered from this analysis. Before all measurements are performed a calibration picture is taken at the same distance. The pixel measurements (both the diameter and centroid position) are converted into meters using the calibration and the velocity is calculated by using the following equation:

$$U_n = \frac{\sqrt{(x_n - x_{n-1})^2 + (y_n - y_{n-1})^2}}{15/fps}$$

In which U_n represents the speed of instance n; x_n and y_n represent the bubble position in meters in relation to the picture's origin at instance n, and fps is the acquisition rate (in frames per second) setting of the high speed. For the presented study, 1000 fps was used.

Bubble diameters was evaluated in different ways, namely by considering an average value for specific working conditions and by following bubble growth rate along the channel. These values were obtained from the analysis of approximately 15 frames, with an accuracy of ±1 pixel.

As for the remaining relevant parameters, uncertainty was evaluated based on Moffat approach [19]. Main uncertainties of the measurements, associated to the equipment are provided in Table 4.

Table 4 – Main uncertainties of the measured parameters

Parameter	**Uncertainty**
Flow rate (Syringe pump)	±0.035%
Inlet pressure	±1.25kPa
Outlet pressure	±0.8kPa
Inlet/outlet temperatures	±0.5ºC
Bubble diameter	±45µm
Bubble Velocity	±0.0029m/s

3. Experimental Results

The experimental results section will resume the findings while analyzing the cases explicit in Table 3. These cases will be referenced by the numbers that identify them in that table.

3.1 Qualitative Analysis of the High-Speed Images

A first look at the high-speed images shows the main differences between the two distinct cases. A set of images were selected and are presented in Figure 3. In Figure 3 a), one can observe very stable and organized flow with few

nucleation sites. The bubbles in this case are constrained by the channel walls and move at near constant speed when fully detached. A nucleation site was detected and is marked by the yellow arrow. Due to the physical restraints of the setup, the camera lens cannot move to the inlet of the channel. It is possible to observe bubbles already formed entering the high-speed camera view range. These bubbles cross the nucleation point, and a small acceleration is visually noticeable. A marked example is the bubble followed by the purple line. Additionally, one can see that the bubble also slightly enlarges due to the coalescence occurring in the nucleation spot region.

Figure 3 b) depicts a slightly more complex flow. Nucleation sites are placed to the left and right of the channel and bubbles can freely pass through each other at different speeds, as a single HFE7100 bubble cannot occupy the whole channel [20]. In blue one can see one such case, a faster bubble collides and coalesces with a slower bubble, and both accelerate due to that. In purple two bubbles approach each other but there is no coalescence. This is probably because they are at different heights. A nucleation site is also visible here and marked in yellow. It is worth noting the higher number of nucleation originating from the same site when compared to the previous example. In this case, the provided heat flux is higher, so a higher nucleation frequency is expected. The main difference between both cases can be stated as the type of flow. Comparing both cases, it is also possible to see an increased number of nucleation sites, as the applied heat flux is higher. Although Case 2 is a textbook example of bubbly flow, Case 1 is a confined bubble flow example as

reported in the work of Yin and Jia [21]. The main parameters that are influencing this difference are clearly the bubble diameter and channel width.

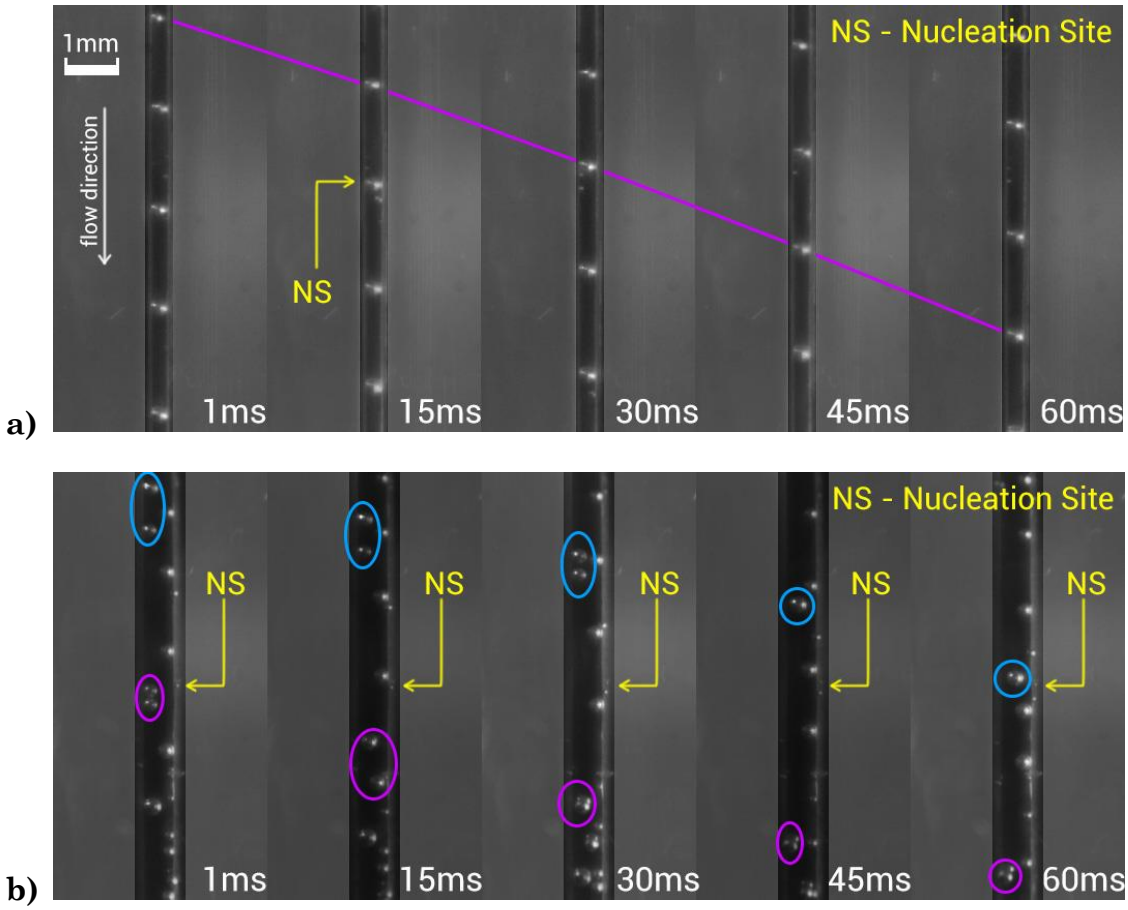

Figure 3 - High Speed Camera frames from the selected cases. a) Case 1; b) Case 2

3.2 Bubble Dynamics during nucleation

Bubble dynamics for both cases will be analyzed by comparing measurements of the bubble diameter and velocity. For both cases, nucleation data was sampled from the very start of nucleation. These parameters were studied as these bubbles reach the end of the camera view range. The study for case 1 is depicted in Figure 4. Isolated bubble growths without coalescence phenomena were picked and an average of the results is presented here. Looking at the

Bubble Velocity graph one can see an almost linear increase of the bubble velocity and then a decrease in acceleration that stabilizes the velocity near 0.12 m/s. While the bubble velocity stabilizes, it's diameter grows closer to the channel diameter until it can grow no further in diameter may transform into a slug if additional coalescence or phase change happens. For Case 2, it is possible to see that the evolution of the bubble diameter is quite similar. Both reach a value close to 400 μm near the 100 ms mark and the growth presents a linear trend. In Case 2, the velocity seems to further increase at the end of the analyzed segment. Here, intensive coalescence phenomena are observed, so the velocity at the end may be influenced by an unseen small bubble merging into the processed ones as the uncertainty grows.

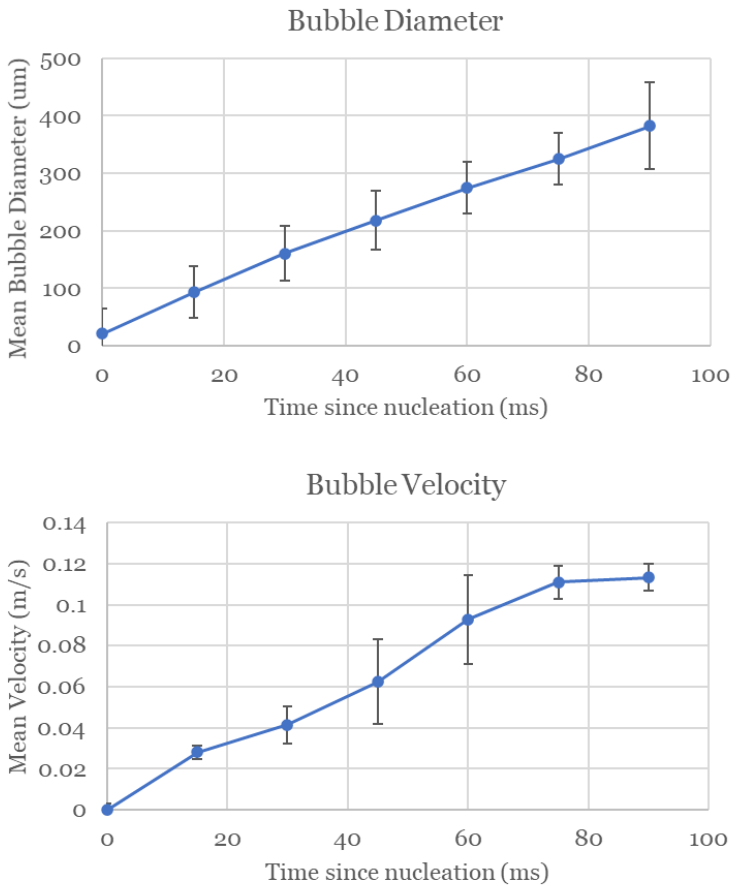

Figure 3 - Bubble Dynamics analysis for case 1: evolution of Bubble Diameter and Bubble Velocity since the start of nucleation

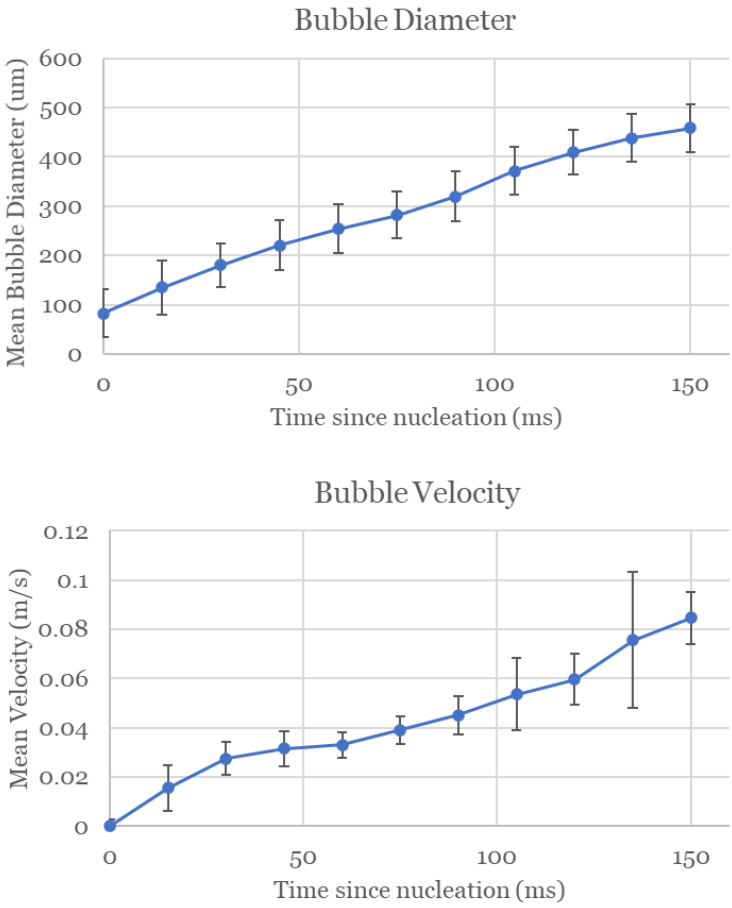

Figure 5 - Bubble Dynamics analysis for case 2: evolution of Bubble Diameter and Bubble Velocity since the start of nucleation

4. Numerical Simulation Methodology

4.1 Governing Equations

A customized enhanced VOF solver that has been developed within the general framework of the open-source toolbox OpenFOAM, has been utilised for the numerical simulations in the present investigation. The enhancements of the solver involve the implementation of: i) an appropriate treatment for spurious velocities dampening (a defect that characterises all VOF methods), ii) a more advanced dynamic contact angle sub-model for

wettability effects iii) an appropriate phase-change model and iv) Conjugate Heat Transfer (CHT) between the two-phase fluid and solid domains. The present sub-section, summarises the main governing equations for mass, momentum, energy, and phase volume fraction. Both liquid and vapour phases are treated as incompressible, Newtonian fluids. This solver has been extensively validated and applied in the past by the authors' research team against various cases of adiabatic and diabatic bubble and droplet dynamics. Further details can be found in [22-28].

The continuity equation is given as:

$$\nabla \cdot \left(\rho \vec{U}\right) = \dot{\rho} \tag{1}$$

where $\vec{U}$ is the fluid velocity and ρ is the bulk mixture density. The term on the right-hand side $\dot{\rho}$ represents the mass source term due to phase change. The momentum equation is given below:

$$\frac{\partial}{\partial t}\left(\rho \vec{U}\right) + \nabla \cdot \left(\rho \vec{U}\vec{U}\right) - \nabla \cdot \left\{\mu \left[\nabla \vec{U} + \left(\nabla \vec{U}\right)^{T}\right]\right\} = -\nabla p + \vec{f}_{ST} + \vec{f}_{g} \tag{2}$$

where p is the pressure and μ is the dynamic viscosity of the bulk mixture. The source terms on the right-hand side account for the effects of surface tension ($\vec{f}_{ST}$) and gravity ($\vec{f}_{g}$) forces, respectively. The surface tension term is modelled with the classical approach of Brackbill et al. [29]. The energy balance in the fluid domain is given by the following equation:

$$\frac{\partial}{\partial t}(\rho c_p T) + \nabla \cdot (\vec{U}\rho c_p T) - \nabla \cdot (\lambda \nabla T) = \dot{h} \quad (3)$$

where c_p is the heat capacity of the bulk mixture, T the temperature field, and λ is the thermal conductivity of the bulk mixture. The term on the right-hand side of the equation ($\dot{h}$) represents a source term for the contribution of the enthalpy of evaporation/condensation that in effect results to the cooling/heating that is associated with the latent heat of the phase-change. The calculated flow field advects the volume fraction α with the use of the following equation:

$$\frac{\partial \alpha}{\partial t} + \nabla \cdot (\alpha \vec{U}) - \nabla \cdot (\alpha(1-\alpha)\vec{U}_r) = \frac{\dot{\rho}}{\rho}\alpha \quad (4)$$

When simulating two-phase flows of two immiscible fluids, the interface sharpening is very important. The sharpening of the interface in OpenFOAM is artificially achieved by introducing the extra compression term $\nabla \cdot (\alpha(1-\alpha)\vec{U}_r)$ in Equation (4) where $\vec{U}_r$ represents the artificial compression velocity. Due to the local mass source terms in the case of evaporation and/or condensation, the velocity field is not free of divergence and therefore, a source term ($\frac{\dot{\rho}}{\rho}\alpha$) is needed on the right-hand side of the Equation (4). Finally, the properties of the bulk fluid mixture are computed as the weighted averages of the liquid and vapor phases. The volume fraction α of each phase is used as the weighting factor (i.e. $\rho = \alpha\rho_l + (1-\alpha)\rho_v$).

As also mentioned previously, the utilised numerical solver has been modified accordingly to account for an adequate level of spurious currents reduction. More details on this implementation to the solver can be found in the paper by Georgoulas et al [22].

The energy balance in the solid domains is described by the following equation:

$$\frac{\partial}{\partial t}\left(\rho_s c_{ps} T\right) = \nabla \cdot (\lambda_s \nabla T) \tag{5}$$

where ρ_s and c_{ps} are the solid domain density and heat capacity, respectively. An iterative coupling at the interface between the fluid and solid domains is conducted ensuring that the following conditions are met:

$$T_f = T_s, \qquad \lambda_f \frac{\partial T_f}{\partial n} = \lambda_s \frac{\partial T_s}{\partial n} \tag{6}$$

where T_f is the temperature at the fluid side of the conjugate heat transfer boundary and T_s is the temperature at the solid side. Finally, λ_f and λ_s are the thermal conductivity of the fluid and solid domains, respectively.

4.2 Phase Change Model

The phase change model originally proposed by Hardt and Wondra [30] has been also implemented in the present OpenFOAM VOF based solver. In more

detail, the evaporation/condensation mass flux at the interface of the two phases (j_{evap}), is calculated with the following equation:

$$j_{evap} = \frac{T_{int} - T_{sat}}{R_{int} h_{lv}} \tag{7}$$

where T_{int} is the interface temperature, T_{sat} is the saturation temperature, R_{int} is the interfacial heat resistance and h_{lv} is the corresponding the latent heat of evaporation/ condensation.

The interfacial heat resistance is calculated using the following formula:

$$R_{int} = \frac{2 - \gamma}{\gamma} \frac{\sqrt{2\pi R_{gas}}}{h_{lv}^2} \frac{T_{sat}^{3/2}}{\rho_v} \tag{8}$$

This equation in effect represents a fitting function since there is a varying uncertainty of the γ parameter that is contained within the range $0 < \gamma < 1$. For all cases presented in the present paper, the parameter γ, which can be referred to as the accommodation coefficient is taken to be equal to 1. R_{gas} represents the specific gas constant of the fluid which is calculated as R/M, where R is the universal gas constant and M is the molecular mass of the fluid.

Then the calculated mass flux is added to the conservation equations, through the calculation of an appropriate volumetric source term. This volumetric

source term is calculated by multiplying the mass flux at the interface by the magnitude of the volume fraction gradient:

$$\dot{\rho}_0 = j_{evap}|\nabla\alpha| \tag{9}$$

The "Net Mass Flow" is then calculated integrating this initially calculated volumetric source term field, through the entire interface:

$$\dot{m}_{int} = \iiint \dot{\rho}_0 \, dV \tag{10}$$

This "Net Mass Flow" is needed to ensure mass conservation. The mass source magnitudes of liquid and vapour should be equal, as they represent the net evaporation rate. In order to avoid computational instabilities, the initially calculated sharp source term is artificially smeared over a finite number of computational cells, through the solution of a diffusion equation:

$$\dot{\rho}_1 - \nabla \cdot [(D\Delta\tau)\nabla\dot{\rho}_1] = \dot{\rho}_0 \tag{11}$$

An artificial time step $\Delta\tau$ is utilised, and Neumann boundary conditions are applied in all boundaries of the domain, for the artificially smeared source term $\dot{\rho}_1$. It should be noted that despite this artificial smearing of the original source term, the integral values of the sharp and the smooth fields remain the same. The width of the smeared field is proportional to the square root of diffusion constant D multiplied by the artificial time step $\Delta\tau$. The selected

value of *D* is in each case adjusted to the mesh resolution, ensuring smearing over a finite number of cells.

The next stage of this process of avoiding computational instabilities, is to take the source terms in all cells that do not contain pure liquid or vapour ($\alpha < 1 - \alpha_{cut}$ and $\alpha > \alpha_{cut}$, where α_{cut} is set to 0.001) and artificially set them to zero in order for the interface containing cells not to be subjected any more to source terms and the interface to be able to be transported only by the calculated velocity field. This makes sure that the transport algorithm for the volume fraction field and the interface compression can work efficiently without any interference with the phase-change source term field. To ensure however continuity, the remaining source term field needs to be scaled on the liquid and the vapour side using appropriate scaling coefficients to ensure that the mass is globally conserved:

$$N_l = \dot{m}_{int} \left[\iiint (a - 1 + a_{cut})\, \dot{\rho}_1 dV \right]^{-1} \tag{12}$$

$$N_v = \dot{m}_{int} \left[\iiint (a_{cut} - a)\, \dot{\rho}_1 dV \right]^{-1} \tag{13}$$

The final source term field is then calculated as:

$$\dot{\rho} = N_v\, (\alpha_{cut} - \alpha)\, \dot{\rho}_1 - N_l (\alpha - 1 + \alpha_{cut})\, \dot{\rho}_1 \,. \tag{14}$$

This particular implementation has been extensively validated by the present Authors' research group in the past [31].

4.3 Dynamic Contact Angle Treatment

The dynamic contact angle (DCA) model originally suggested by Kistler [32], has also been utilised in the numerical simulation solver that is used for the simulations of the present investigation. The proposed implementation has been validated in the past against experiments available in the literature for droplet impact on flat surfaces with different wettability [24] as well as against experiments of pool boiling in biphilic surfaces [33], with excellent degree of convergence between the experimental measurements and the numerical predictions. Furthermore, it has been recently applied for the investigation of the effect of wettability in flow boiling characteristics within microchannels by the same Authors' team as the present paper [26].

In more detail, the dynamic contact angle θ_d is given as a function of the contact line velocity (u_{cline}), through the capillary number Ca and the inverse of Hoffman's function:

$$\theta_d = f_H\left[Ca + f_H^{-1}\left(\theta_{eq}\right)\right] \tag{15}$$

where f_H^{-1} is the inverse function of the Hoffman's empirical function calculated as:

$$f_H = \arccos\left\{1 - 2\tanh\left[5.16\left(\frac{x}{1 + 1.31x^{0.99}}\right)\right]^{0.706}\right\} \tag{16}$$

where x is given by:

$$x = f_H \left[Ca + f_H^{-1} \left(\theta_{eq} \right) \right] \quad (17)$$

And the capillary number is defined as:

$$Ca = \frac{\mu u_{cline}}{\sigma} \quad (18)$$

The equilibrium angle θ_{eq} is replaced by either a limiting advancing or receding contact angle θ_a or θ_r, according the sign of the velocity vector at the contact line position.

5. Application of Numerical Model

5.1. Computational Geometry, Mesh and Boundary Conditions

In Figure 6, the generated computational geometry, mesh and the applied boundary conditions are illustrated. The computational domain has been discretised in two different parts; the solid domain and the fluid domain. A, structured computational mesh, with uniform cell sizes consisting of hexahedral elements is used. An element size of 4 μm was selected following a mesh independency study that has been performed in a recent, previous work [28], and therefore it will be not be further described here. Two different microchannel geometries are considered, a narrow channel (width to height aspect ratio β=0.5) and a wide channel (width to height aspect ratio β = 1.0). The height and length of the considered fluid and solid domains are kept

constant. The total number of cells of the solid domain for the β =0.5 and β =1.0 microchannels are 0.75M and 1.5M cells, respectively, while for the fluid domains 37.5 M and 75.0 M cells, respectively. The fluid domain dimensions (length, height, and width) are L_f = 4.8 mm, H_f = 1 mm, W_f = 0.5, 1.0 mm, and the solid domain dimensions are L_s = 4.8 mm, H_s = 0.02 mm, W_s = 0.5, 1.0 mm. Only the first 4.8 mm of the corresponding experimental channels are considered and studied for the numerical simulations due to the increased computational cost.

β	L_s [mm]	H_s [mm]	W_s [mm]	Cell No.	L_f [mm]	H_f [mm]	W_f [mm]	Cell No.
0.5	4.8	0.02	0.5	0.75M	4.8	1.0	0.5	37.5M
1.0	4.8	0.02	1.0	1.5M	4.8	0.02	1.0	75.0M

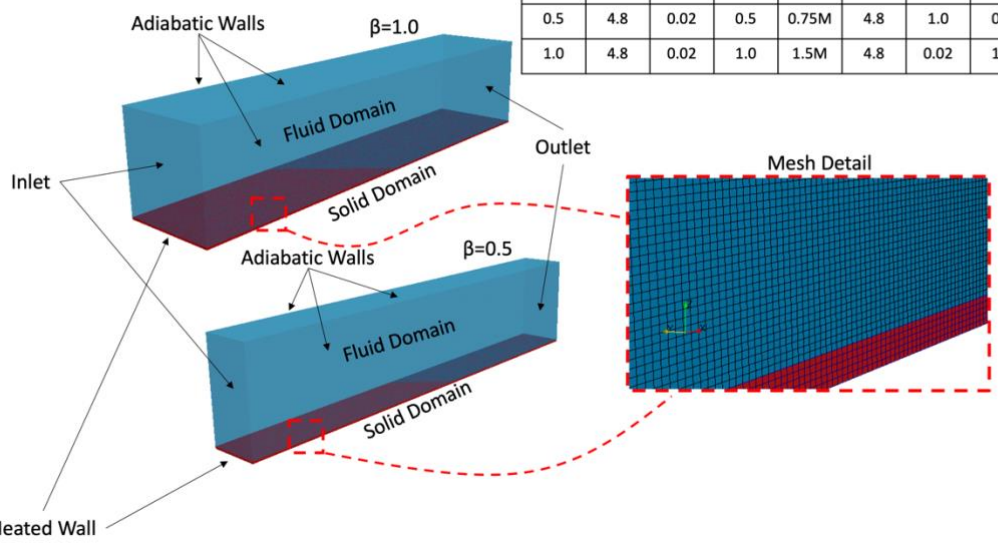

Figure 6 - Computational domain, boundary conditions and mesh details

Apart from the inlet and outlet in the fluid domain and the bottom side of the solid domain, where a constant heat flux is applied, all the rest surfaces are considered to be adiabatic walls. At the walls, a standard no-slip velocity boundary condition was used with a fixed flux pressure boundary condition for the pressure values. Moreover, a dynamic contact angle boundary

condition is imposed for the volume fraction field, by assigning the maximum advancing and minimum receding contact angles. For the sidewalls of the fluid and solid domains, as well as for the top wall of the fluid domain a zero gradient boundary condition was used for the temperature field. At the outlet, a fixed-value pressure boundary condition and a zero-gradient boundary condition for the volume fraction were used, while for the velocity values a hybrid type of boundary condition was imposed that applies a zero-gradient, when the fluid mixture exits the computational domain and a fixed value condition to the tangential velocity component when the fluid mixture enters the computational domain. A zero gradient boundary condition for the temperature field was also prescribed at the outlet boundary. For the inlet, a uniform constant velocity value was applied as well as a fixed flux pressure condition. The volume fraction value was assigned as unity, as saturated liquid only enters from the inlet during the calculations. The temperature of the liquid at the inlet was also fixed at the saturation temperature. At the CHT interface both the temperature values as well as the heat fluxes are coupled, for each calculation time step, following an inner iteration process.

5.2. Numerical Simulation Set-up and Procedure

Two main stages are followed for all simulations. During the first stage, a specified heat flux is applied to the heated boundary of the solid domain, and a single-phase saturated liquid flow is considered initially with a specific flow rate. This is run up to a steady state condition where both the initial hydrodynamic and thermal boundary layers have been developed. At the

second stage, 60 arbitrary distributed bubble seeds are placed simultaneously on the conjugate heat transfer boundary, in the form of half-spheres with a radius of 20 μm (Figure 7). This was decided due to the absence of experimental information close to the inlet of the channels as the experimental images were recorded at a further downstream region. At this point it should be stated that in the future a nucleation site density, location and frequency sub-model must be used, in order to better account for the nucleation characteristics with respect to the flow conditions.

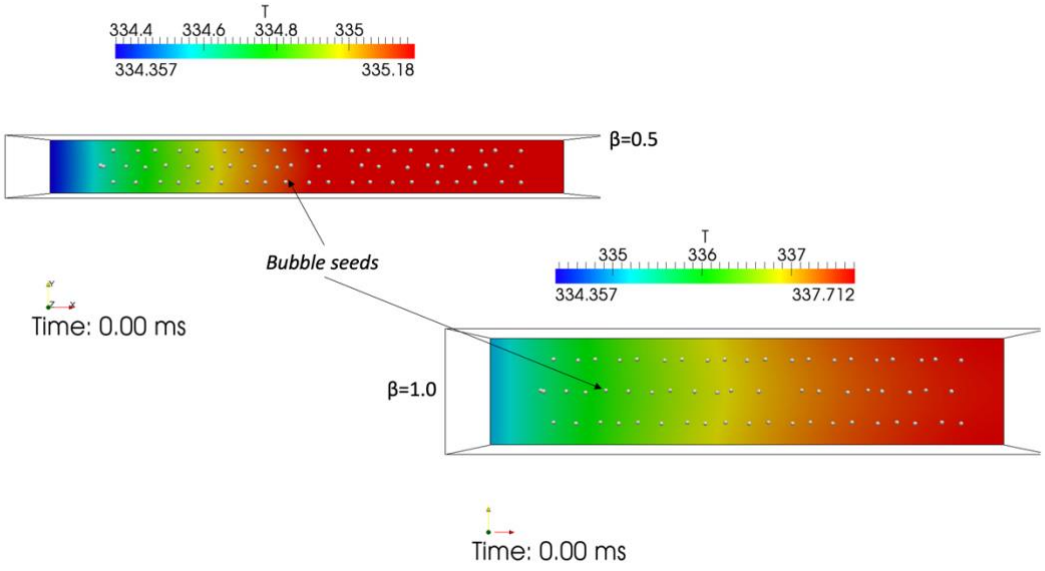

Figure 7 - Initial condition for the second (two-phase) stage of numerical simulations for each of the considered channels.

It should be mentioned that for both simulations the liquid and vapour phase properties are taken as these of HFE7100 liquid and vapour at the saturation equilibrium point for a pressure of P_{sat} = 1 bar, which corresponds to a saturation temperature of T_{sat} = 334.15 K (REFPROP NIST software [37]).

The advancing (θ_a) and receding (θ_r) contact angles were taken according to Table 1.

A High-Performance Computing (HPC) cluster was utilized for these two numerical runs. Each run required 400 computational cores. The duration of the computation for each of the 2 single phase stage simulations (one for each channel aspect ratio) was approximately 15 days, as a few seconds of real flow were required for a steady state condition to be reached. For the corresponding two-phase simulation stages, the duration of the computation was 7 days since just a few milliseconds of real flow were required. In total 422,400 core-hours were utilized for the final runs. It should be mentioned that a variable calculation time step was utilized for all runs with the courant number kept constant at 0.5 for the two-phase simulations and 1.0 for the single-phase simulations. For the two-phase simulations, the calculation time step was varied automatically, ranging from approximately 10^{-8} up to 10^{-6} s while for the single-phase simulations it was also varied automatically, ranging from approximately 10^{-6} up to 10^{-5} s.

6. Numerical Simulation Results

The spatial and temporal evolution of the generated vapor bubbles for each channel case are depicted in Figures 8 and 9, for four successive time instances. The grey surface represents the liquid/vapor interface, while the colored contours reveal the instantaneous temperature fields.

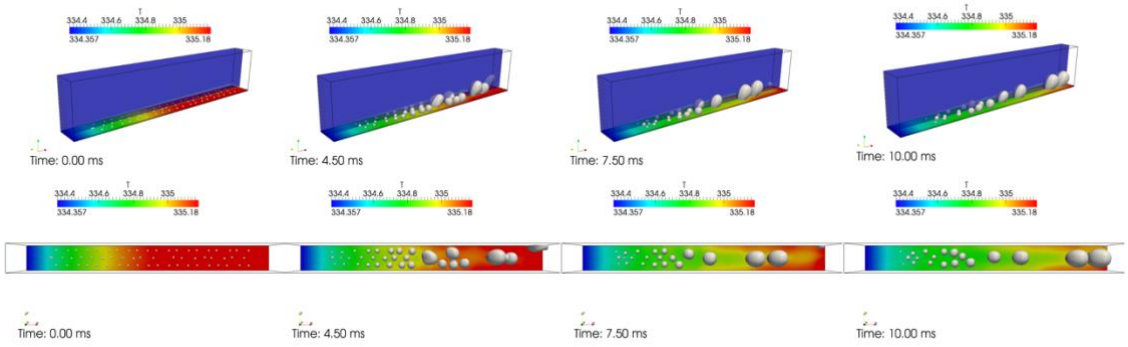

Figure 8. Isometric view and top view of spatial and temporal evolution of the generated vapour bubbles (β=0.5)

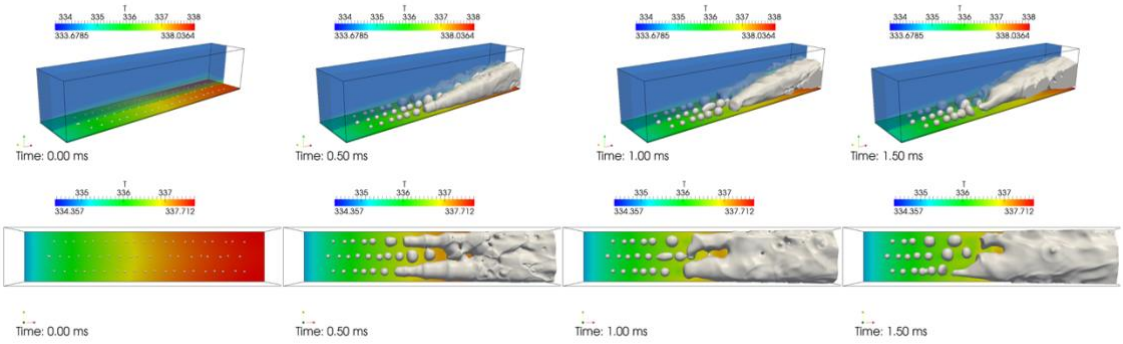

Figure 9. Isometric view and top view of spatial and temporal evolution of the generated vapour bubbles (β=1.0)

It is evident that the variation of the channel aspect ratio as well as of the applied heat flux and mass flux has a significant effect in the generated two-phase flow regimes. For the assumed arbitrary initial distribution of the 60 nucleation sites, it is clear that for the narrow channel (β = 0.5) the bubbles grow in contact with the heated wall and coalescence into bigger bubbles, indicating the transition from a bubbly to a slug plug regime which is also evident from the high-speed images of the corresponding experimental run. On the contrary, in the case of the square channel, due to the higher initial superheat the bubbles grow faster and coalesce, indicating the transition from a bubbly flow regime to a churn flow regime. This has not been observed in

the corresponding experimental run, where a bubbly flow regime is evident from the high-speed images. This difference might be attributed to the initial assumed density and position of the nucleation sites (bubble seeds) in the numerical simulation that might differ significantly from the actual initial situation in the experiments. However, as it has been mentioned previously the experimental images are taken at downstream section of the channels and it was not possible to estimate the nucleation site density and position for the inlet section of the microchannels where the numerical simulations are focused. Despite this fact, the proposed numerical simulation predictions indicate that the utilised numerical simulation methodology is able to capture the effects of variations in the channel cross-section, the applied heat flux as well as the applied mass flux in the generated bubble dynamics and heat transfer characteristics and it can therefore constitute an important investigation tool that can give additional insight in the further understanding of the experimental measurements. For the future, however, it is vital to better estimate the initial condition regarding the nucleation site density and position the experimental runs.

In order to also quantify the effects of the variation of the channel aspect ratio, applied heat flux and mass flux in the heat transfer characteristics, the time averaged local Nusselt number is plotted against the dimensionless channel length in Figure 10. The corresponding single-phase curves (first stage of numerical simulations) is also plotted as a reference in each case. As it can be observed, the bubbly to slug-plug flow transition that has been

predicted numerically for the narrow channel case has resulted in a significant increase in the local heat transfer in comparison to the single-phase stage (Fig 10 (a)). On the contrary, the direct transition from a bubbly to a churn flow regime for the square channel case has resulted in less significant increase of the local heat transfer in comparison to the single phase stage (Fig10 (b)). This is due to the fact that in the slug-plug flow regime there is a combination of contact line evaporation and liquid film evaporation. Additionally, in the case of the churn flow regime the existing liquid films between the vapour regions and the heated wall become highly unstable and therefore the contribution of the liquid film evaporation mechanism in the overall heat transfer is significantly lower than that in the case of slug-plug flow. It is also evident that the single-phase stage of the narrow channel results in significantly higher local Nusselt numbers in comparison to the single-phase stage of the square channel. This can probably be attributed to the higher mass flow rate in the case of the narrow channel (Table 3).

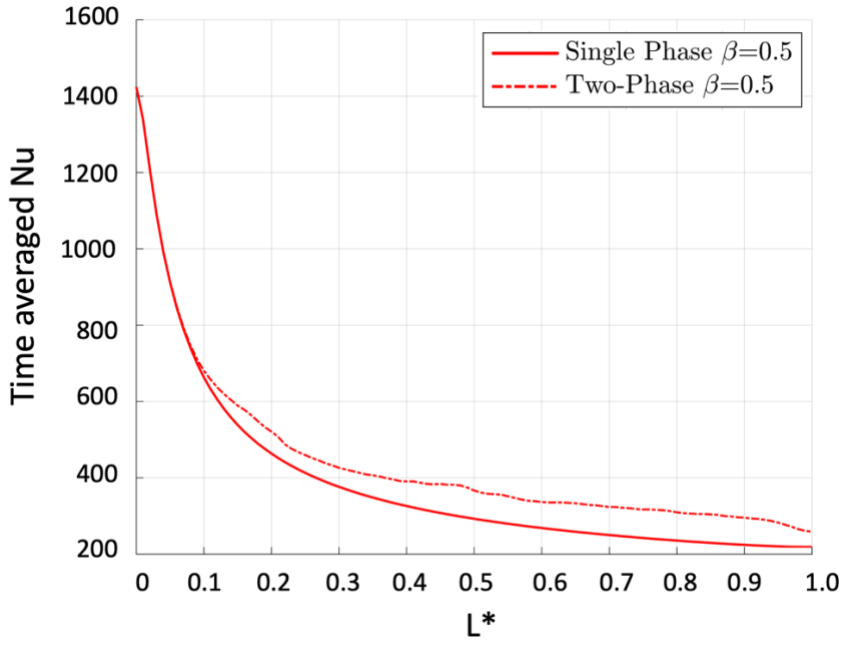

(a)

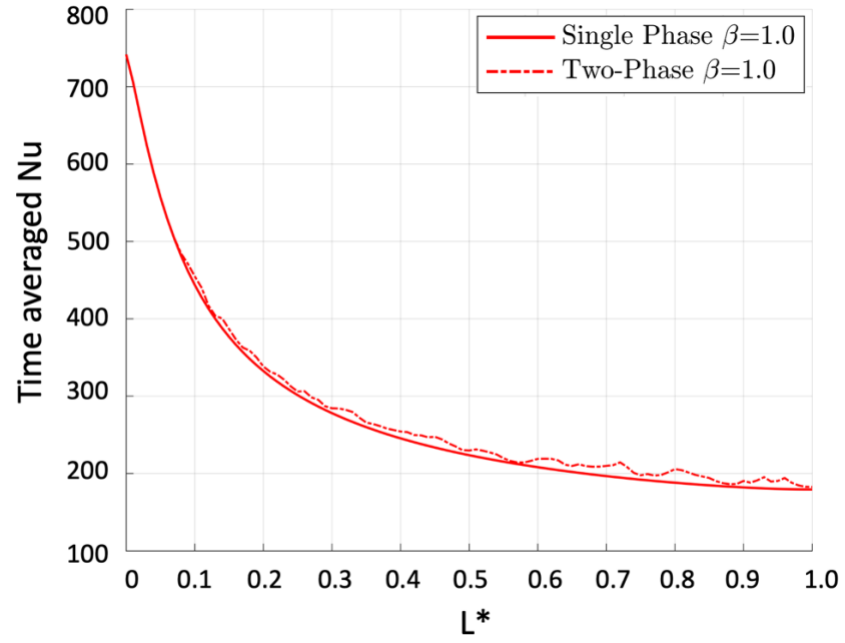

(b)

Figure 10. Time averaged Nusselt number along the conjugate heat transfer boundary as a function of dimensionless length. (a) β=0.5, (b) β=1.0.

7. Conclusions

In this work two different approaches aimed at getting a better understanding of the phenomena occurring in flow boiling based microchannel cooling at similar conditions.

A first approach, by experimental means, aimed at observing the effects of the channel width, heat flux and flowrate in the flow, bubble diameter and bubble speed. Two types of flow were observed. The first in a smaller channel, constrained by the width was categorized as a confined bubble flow. The second, a bubbly flow, while unrestrained, showed more coalescence phenomena, but also higher nucleation sites by means of a lower flowrate and higher heat flux. While the technique used was able to provide valuable insight, the top view in this case is very restrictive. The detachment of the bubbles from the surface cannot be properly recorded and the dynamic parameters evaluated are influenced by unseen coalescence phenomena on the vertical axis. Here one can benefit from a side view as it can provide further information on the bubble dynamics. But it is also here where the numerical work can add significant value, even analyzing higher complexity flows that are impossible to characterize visually.

Hence, a second approach, by numerical means, aimed therefore, to apply an enhanced customized VOF-based numerical simulation framework (that accounts for spurious currents reduction (a well-known defect of VOF methods), phase-change, accurate dynamic contact angle modelling and conjugate heat transfer between solid and two-phase fluid domains) for the prediction of the first transient stages of the two-phase flow development

close to the inlet of the microchannels. An arbitrary distribution and density of nucleation sites were considered, since the experimental measurements focus was in a further downstream part of the considered channels. The numerical predictions reveal that the proposed numerical simulation tool is sensitive enough to capture the effects of channel aspect ratio, applied heat flux and mass flux in the transient generated bubble dynamics and heat transfer characteristics. The predicted trends for the results are in good qualitative agreement with the experimental observations for the narrow channel, since a transition from bubbly flow to slug plug flow is numerically predicted. However, the numerically predicted transition from bubbly flow to churn flow is not in agreement with the experimental measurements of the square channel case. This is attributed to the assumed nucleation site distribution for the numerical runs that was not probably appropriate for the square channel case. Therefore, for future investigation it is vital to better estimate the initial condition of the numerical simulations from the experimental runs. This will lead in better qualitative and quantitative agreement between experiments and simulations that will lead to more quantitative conclusions regarding the bubble dynamics and heat transfer characteristics of such complex micro-scale flows that can eventually contribute to the development of accurate design correlations of industrial design relevance.

Acknowledgements

Authors acknowledge to Fundação para a Ciência e Tecnologia (FCT) for partially financing the research through project PTDC/EMETED/7801/2020 and to Portuguese Army – Ministério da Defesa, for financing project CINAMIL nº 02_2021 - Development of thermal management and climatization systems for CBRN equipment. Mr. Pedro Pontes also acknowledges to FCT for supporting his PhD fellowship (Ref. SFRH/BD/149286/2019).

The numerical part of this research was partially funded through the European Space Agency (ESA MAP CORA projects TOPDESS and ENCOM4). Finally, Dr. Georgoulas and Dr. Andredaki would like to specifically thank also University of Brighton for the financial support through the Rising Stars Initiative Scheme and more particularly the School of Architecture Technology and Engineering for providing simulation time in its High-performance Computing Facilities

References

[1] NREL, "Best research-cell efficiency chart," 2019. https://www.nrel.gov/pv/cell-efficiency.html, Accessed on 2 February 2022.

[2] S. Kurtz et al., "Opportunities and challenges for development of a mature concentrating photovoltaic power industry," 2009.

[3] A. Royne, C. J. Dey, and D. R. Mills, "Cooling of photovoltaic cells under concentrated illumination: a critical review," Solar energy materials and solar cells, vol. 86, no. 4, pp. 451–483, 2005.

[4] D. B. Tuckerman and R. F. W. Pease, "High-performance heat sinking for vlsi," IEEE Electron Device Letters, vol. 2, no. 5, pp. 126–129, 1981.

[5] X. Peng and G. Peterson, “Convective heat transfer and flow friction for water flow in microchannel structures,” International journal of heat and mass transfer, vol. 39, no. 12, pp. 2599–2608, 1996

[6] G. Xia, D. Ma, Y. Zhai, Y. Li, R. Liu and M. Du. “Experimental and numerical study of fluid flow and heat transfer characteristics in microchannel heat sink with complex structure”. Energy Conversion and Management, 105, pp.848-857, 2015.

[7] H. Wang, Z. Chen, and J. Gao, “Influence of geometric parameters on flow and heat transfer performance of microchannel heat sinks,” Applied Thermal Engineering, vol. 107, pp. 870–879, 2016.

[8] D. Raghuraman, R.T.K. Raj, P. Nagarajan and B. Rao. “Influence of aspect ratio on the thermal performance of rectangular shaped micro channel heat sink using CFD". Alexandria Engineering Journal, 5643–54, 2017

[9] X.L. Xie, Z.J. Liu, Y.L. He, and W.Q. Tao. “Numerical study of laminar heat transfer and pressure drop characteristics in a water-cooled minichannel heat sink”. Applied thermal engineering, 29(1), pp.64-74., 2009

[10] G. Hetsroni, A. Mosyak, Z. Segal, and G. Ziskind. “A uniform temperature heat sink for cooling of electronic devices” International Journal of Heat and Mass Transfer, vol. 45, n. 16, pp. 3275–3286, 2002.

[11] T. N. Tran, M. W. Wambsganss and D. M. France, “Small circular-and rectangular-channel boiling with two refrigerants”, Int. J. Multiph. Flow, vol. 22, n. 3, pp. 485–498, 1996.

[12] V. S. Koscheyev, G. R. Leon, S. Paul, D. Tranchida, I. V. Linder. "Augmentation of blood circulation to the fingers by warming distal body areas". Eur. J. Appl. Physiol., 82:103–111, 2000

[13] H. Cao, D.H. Branson, S. Peksoz, J. Nam, C. A. Farr. "Fabric selection for a liquid cooling garment". Textile Res. J., 76(7): 587–595, 2006.

[14] G. Bartkowiak, A. Dabrowska and A. Marszalek. "Assessment of an active liquid cooling garment intended for use in a hot environment". Applied Ergonomics, 58:182–189, 2017.

[15] K. Tokizawa, S.-Y. Son, T. Oka and A. Yasuda, "Effectiveness of a field-type liquid cooling vest for reducing heat strain while wearing protective clothing". Industrial Health, 58:63-71, 2020.

[16] P. Pontes, R. Cautela, E. Teodori, A. S. Moita, Y. Liu, A. L. N. Moreira, A. Nikulin and E. Del Barrio. "Effect of pattern geometry on bubble dynamics and heat transfer on biphilic surfaces". Experimental Thermal and Fluid Science, 115(1):110088, 2020

[17] P. Pontes, R. Cautela, E. Teodori, A. S. Moita, A. L. N. Moreira. "Experimental description of bubble dynamics and heat transfer processes occurring on the pool boiling of water on biphilic surfaces". Applied Thermal Engineering, 178:1155507, 2020

[18] L. E.W., I. H. Bell, M. L. Huber, and M. O. McLinden, 'REFPROP Documentation Release 10.0'. 2018.

[19] R. J. Moffat, "Describing the uncertainties in experimental results", Exp. Therm. Fluid Sci., vol. 1, n. 1, 3–17, 1988.

[20] A.S. Moita, E. Teodori, A.L.N. Moreira, A. L. N., “Influence of surface topography in the boiling mechanisms”. International Journal of Heat and Fluid Flow, vol. 52, 50-63, 2015.

[21] L. Yin, and L. Jia. "Confined bubble growth and heat transfer characteristics during flow boiling in microchannel." International Journal of Heat and Mass Transfer 98, 114-123, 2016

[22] A. Georgoulas, P. Koukouvinis, M. Gavaises, and M. Marengo, ‘Numerical investigation of quasi-static bubble growth and detachment from submerged orifices in isothermal liquid pools: The effect of varying fluid properties and gravity levels’, Int. J. Multiph. Flow, vol. 74, pp. 59–78, 2015, doi: 10.1016/j.ijmultiphaseflow.2015.04.008.

[23] A. Georgoulas, M. Andredaki, and M. Marengo, ‘An enhanced VOF method coupled with heat transfer and phase change to characterise bubble detachment in saturated pool boiling’, Energies, vol. 10, no. 3, 2017, doi: 10.3390/en10030272.

[24] E. Teodori, P. Pontes, A. Moita, A. Georgoulas, M. Marengo, and A. Moreira, ‘Sensible heat transfer during droplet cooling: Experimental and numerical analysis’, Energies, vol. 10, no. 6, 2017, doi: 10.3390/en10060790.

[25] K. Vontas, M. Andredaki, A. Georgoulas, K. S. Nikas, and M. Marengo, ‘Numerical Investigation of Droplet Impact on Smooth Surfaces with Different Wettability Characteristics: Implementation of a dynamic contact angle treatment in OpenFOAM’, in 28th European Conference on Liquid Atomization and Spray Systems, 2017, doi: http://dx.doi.org/10.4995/ILASS2017.2017.5020.

[26] P. Pontes, R. Cautela, E. Teodori, A. S. Moita, A. Georgoulas, and A. L. N. M. Moreira, 'Bubble Dynamics and Heat Transfer on Biphilic Surfaces: Experiments and Numerical Simulation', J. Bionic Eng., 2020, doi: 10.1007/s42235-020-0064-x.

[27] M. Andredaki, A. Georgoulas, N. Miché, and M. Marengo, 'Accelerating Taylor bubbles within circular capillary channels: Break-up mechanisms and regimes', Int. J. Multiph. Flow, vol. 134, 2021, doi: 10.1016/j.ijmultiphaseflow.2020.103488.

[28] K. Vontas, M. Andredaki, A. Georgoulas, N. Miché, and M. Marengo, 'The effect of surface wettability on flow boiling characteristics within microchannels', Int. J. Heat Mass Transf., vol. 172, p. 121133, 2021, doi: https://doi.org/10.1016/j.ijheatmasstransfer.2021.121133.

[29] J. Brackbill, D. Kothe, and C. Zemach, 'A continuum method for modeling surface tension', J. Comput. Phys., vol. 100, no. 2, pp. 335–354, Jun. 1992, doi: 10.1016/0021-9991(92)90240-Y.

[30] S. Hardt and F. Wondra, 'Evaporation model for interfacial flows based on a continuum-field representation of the source terms', J. Comput. Phys., vol. 227, no. 11, pp. 5871–5895, 2008, doi: 10.1016/j.jcp.2008.02.020.

[31] A. Georgoulas, M. Andredaki, and M. Marengo, 'An Enhanced VOF Method Coupled with Heat Transfer and Phase Change to Characterise Bubble Detachment in Saturated Pool Boiling', Energies, vol. 10, no. 3, p. 272, Feb. 2017, doi: 10.3390/en10030272.

[32] S. F. Kistler, 'In Hydrodynamics of Wetting', in Wettability, no. 1993, J. C. Berg, Ed. (Dekker, New York, 1993), 1993, pp. 311-429.

[33] P. Pontes, R. Cautela, E. Teodori, A. Moita, A. Georgoulas, and A. L. N. Moreira, 'Bubble dynamics and heat transfer on biphilic surfaces', in Proceedings of the 16th UK Heat Transfer Conference (UKHTC2019), p.3, 2019.